

## Two-phase mixture of iron–nickel–silicon alloys in the Earth’s inner core

Daijo Ikuta<sup>1</sup> , Eiji Ohtani<sup>1</sup>  & Naohisa Hirao<sup>2</sup> 

The Earth’s inner core comprises iron–nickel alloys with light elements. However, there is no clarity on the phase properties of these alloys. Here we show phase relations and equations of state of iron–nickel and iron–nickel–silicon alloys up to 186 gigapascals and 3090 kelvin. An ordered derivative of the body-centred cubic structure (B2) phase was observed in these alloys. Results show that nickel and silicon influence the stability field associated with the two-phase mixture of B2 and hexagonal close-packed phases under core conditions. The two-phase mixture can give the inner core density of the preliminary reference Earth model. The compressional wave velocity of the two-phase mixture under inner core conditions is consistent with that of the preliminary reference Earth model. Therefore, a mixture of B2 and hexagonal close-packed phases may exist in the inner core and accounts for the seismological properties of the inner core such as density and velocity deficits.

<sup>1</sup>Department of Earth Science, Tohoku University, Sendai, Miyagi 980-8578, Japan. <sup>2</sup>Japan Synchrotron Radiation Research Institute, Sayo, Hyogo 679-5198, Japan. ✉email: [dikuta@tohoku.ac.jp](mailto:dikuta@tohoku.ac.jp); [eohtani@tohoku.ac.jp](mailto:eohtani@tohoku.ac.jp)

The Earth's inner core contains iron (Fe) as the main component and approximately 5–10 weight percent (wt%) of nickel (Ni)<sup>1,2</sup>. However, it is well known that the density of the inner core is approximately 4% lower than that of pure hexagonal close-packed (hcp) iron<sup>3</sup> or approximately 5% lower than that of Fe–Ni alloys<sup>4</sup> under inner core conditions. Therefore, the inner core is considered to contain certain light elements. Silicon (Si) is one of the most plausible light elements to be considered as a part of the inner core composition because it exists in the form of iron alloys in iron meteorites and is depleted in the Earth's mantle when compared to its abundance in chondrites<sup>5</sup>.

Nickel, together with silicon can affect the phase relations of iron alloys. Based on theoretical calculations (e.g., ref. 6) and high-pressure experiments such as those conducted with Fe–10.5wt%Ni (Fe–10.5Ni) alloy<sup>7</sup> and Fe–Si alloys<sup>8–12</sup>, it has been suggested that a body-centred cubic (bcc) or B2 (ordered derivative of bcc) phase may exist in the inner core. However, recent work on the phase relation of the Fe–5wt%Ni–4wt%Si system showed the existence of only the hcp phase up to 200 GPa and 3900 K<sup>13</sup>. Therefore, the existence of a stable B2 (or bcc) structure of iron alloys in the inner core remains under debate. Furthermore, coexistence of B2 and hcp phases has been observed in Fe–Si alloys with a silicon content of >6 wt%<sup>10</sup>.

In this study, we investigate the effects of silicon and nickel on the phase relations in the Fe–Ni–Si system under core conditions. Results show that the two-phase mixture elucidates the inner core density of the preliminary reference Earth model (PREM). The compressional wave velocity ( $v_p$ ) of the two-phase mixture under inner core conditions is consistent with that of the PREM. It is concluded that the inner core may be composed of a mixture of B2 and hcp phases, which explains the seismological properties of the inner core in terms of its density and velocity deficits.

## Results

The conditions and the results of in situ X-ray diffraction experiments are listed in Supplementary Data 1 [Fe–7wt%Ni (Fe–7Ni)], Supplementary Data 2 [Fe–7wt%Ni–5wt%Si (Fe–7Ni–5Si)], Supplementary Data 3 [Fe–7wt%Ni–9wt%Si (Fe–7Ni–9Si)], and Supplementary Data 4 [Fe–7wt%Ni–15wt%Si (Fe–7Ni–15Si)]. Typical X-ray diffraction patterns are shown in Fig. 1a, b (Fe–7Ni alloy at ~185 GPa and ~2900 K), Fig. 1c (Fe–7Ni–9Si alloy at ~130 GPa and 1350–1700 K), and Fig. 1d (Fe–7Ni–15Si alloy at 97–116 GPa and 300–2800 K). We observed the appearance of a mixture of B2 and hcp phases (Fig. 1a–c). Typical diffraction peaks of the B2 phase (100, 110, 111, and 200 on the Miller indices) appeared at temperatures between 2850 and 2970 K at ~185 GPa in Fe–7Ni system (Fig. 1b), and between 1350 and 1700 K at ~130 GPa in Fe–7Ni–9Si system (Fig. 1c). The B2 phase was identified by the presence of 100 and/or 111 peaks, which are not observed in the disordered bcc structure but are characteristic diffraction peaks of B2 (ordered bcc structure). A phase transition was not observed in the Fe–7Ni–15Si system at 97–116 GPa (Fig. 1d) in all the temperature range studied.

Figure 2a shows the phase relation of the Fe–7Ni system. The B2 and hcp phases were observed at temperatures above 2500 K; these data indicate that the hcp Fe–7Ni alloy decomposes at high temperatures without pressure dependence or with a low boundary slope. The equations of state (EoS) of B2 and hcp phases for the Fe–7Ni system are shown in Fig. 3a, b, respectively. The B2 phase has a volume that is approximately 6% larger than that of the hcp phase, as shown in Fig. 3a. The molar volume of B2 phase is consistent with that of the bcc phase in the Fe–10.5Ni alloy at 225 GPa and 3400 K<sup>7</sup> (Fig. 3a).

Figure 2b shows the phase relation of the Fe–7Ni–5Si system. A single hcp phase was observed over all pressure ranges studied below 2300 K, and coexistence of the B2 and hcp phases was observed above this temperature. The boundary of the decomposition of the hcp phase to the B2 and hcp phases displayed extremely weak positive slopes at 2300–2500 K. The EoS of the B2 and hcp phases for the Fe–7Ni–5Si system are shown in Fig. 3c, d, respectively.

Figure 2c shows the phase relation of the Fe–7Ni–9Si system. A single hcp phase was observed in all the pressure ranges studied below 1700 K, and the coexistence of the B2 and hcp phases was observed above this temperature. The boundary of the decomposition of the hcp phase to the B2 and hcp phases exhibits a very weak positive slope at 2300–2500 K. The EoS of the B2 and hcp phases for the Fe–7Ni–9Si system are shown in Fig. 3e, f, respectively. The molar volume of the B2 phase was approximately 3% larger than that of the hcp phase, as shown in Fig. 3e.

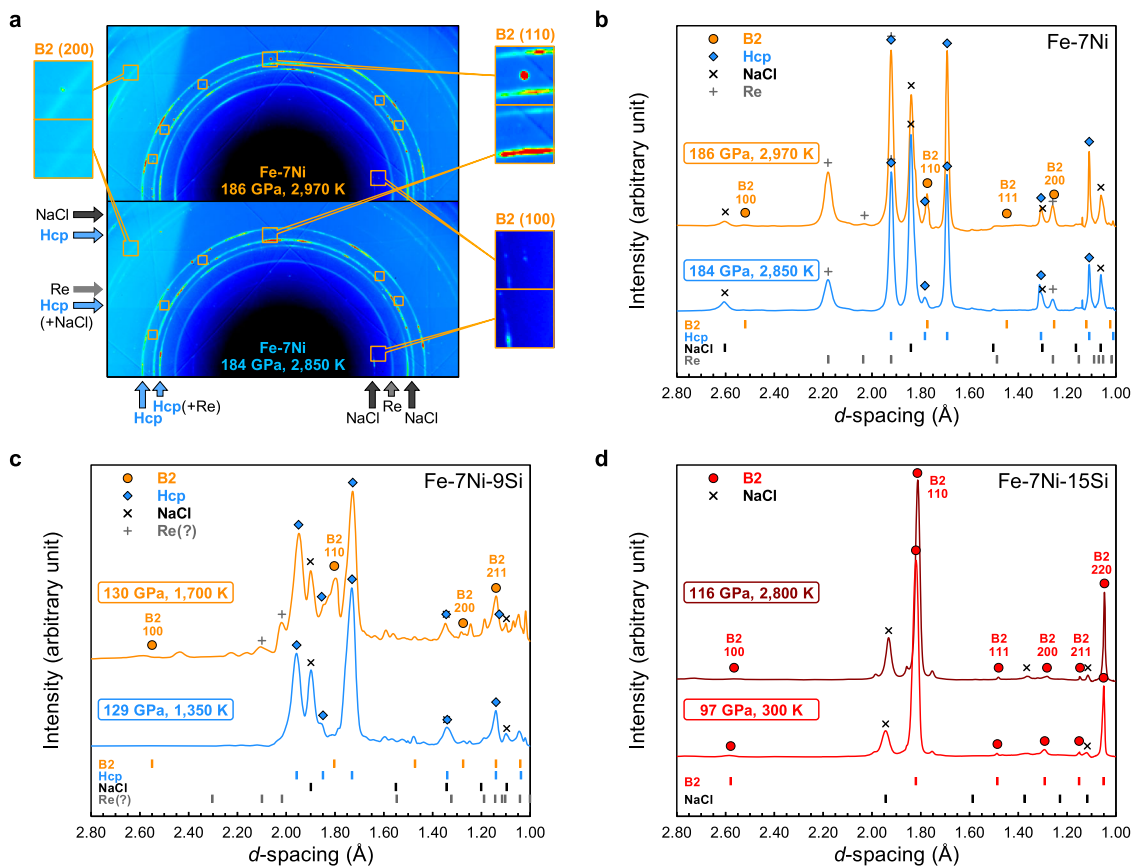
Figure 2d shows the phase relation of the Fe–7Ni–15Si system; this system is different from the above three systems. The single-ordered derivative of bcc phase was observed in all the studied regions. Another ordered derivative of the bcc phase (D0<sub>3</sub> phase) was observed at pressures below 25 GPa at all temperatures to 2000 K. On the other hand, the B2 phase was observed in the pressure range from 35 to 120 GPa at all temperatures. The boundary of the D0<sub>3</sub> and B2 phases at 30–40 GPa has a positive slope with a small temperature dependence. The EoS of the D0<sub>3</sub> and B2 phases for the Fe–7Ni–15Si system are shown in Fig. 3g.

Figure 3h shows the molar volumes of the B2 and hcp phases under the inner core boundary (ICB) conditions (approximately 330 GPa and 6000 K), which were estimated by extrapolation of the EoS determined here. For all the studied bulk compositions, the volumes of the two phases were nearly the same (~4.2 cm<sup>3</sup> mol<sup>-1</sup>) within the error ranges. The EoSs of the hcp phase were estimated by those of the single hcp phase observed at lower temperatures in the Fe–Ni–Si system (see Fig. 2). The silicon content of the B2 phase, especially for Fe–7Ni–5Si and Fe–7Ni–9Si, may not be the same as that of the bulk compositions since it appeared at high temperature coexisting with the hcp phase.

## Discussion

Large modifications of the phase relations of iron were observed after the alloying of nickel and silicon in iron. Figure 4 shows the composition–pressure diagrams at several different temperatures from 1700 K to 2700 K and indicates the thermodynamic consistency of the stability of B2 and hcp phases.

Although the coexistence of the B2 and hcp phases is consistent with that in the Fe–Si system<sup>10,14</sup>, the present results have revealed that large differences are observed after the addition of nickel in pure iron; i.e., the hcp alloy is decomposed into a mixture of B2 and hcp at high pressures and temperatures above 2700 K (below the melting temperature) in the Fe–7Ni alloy (Fig. 2a). The phase relations in the Fe–7Ni–9Si system are different from those in the Fe–9wt%Si system<sup>10,14</sup>. Furthermore, the Fe–7Ni–9Si system exhibited a wide region of the two-phase mixture of B2 and hcp phases at temperatures above 1700 K, which is included in the single hcp phase region in the Fe–9wt%Si system. Another difference has been observed in the Fe–7Ni–15Si system compared with the Fe–16wt%Si system<sup>10,14</sup>; i.e., the stability field of the single B2 phase was wider and there was no field associated with the coexistence of the B2 and hcp phases in the Fe–7Ni–15Si system, whereas the Fe–16wt%Si system exhibited a field associated with the two-phase mixture at high pressures and temperatures.



**Fig. 1** Typical X-ray diffraction patterns of Fe-7Ni, Fe-7Ni-9Si, and Fe-7Ni-15Si at high pressure and temperature. **a** Two-dimensional diffraction patterns collected at 184 GPa and 2850 K and 186 GPa and 2970 K. Orange squares represent the appearance of typical peaks for the B2 phase of Fe-Ni. Blue and grey arrows indicate the diffraction of the hcp phase of Fe-Ni, sodium chloride (NaCl) and rhenium (Re). Integrated diffraction patterns of **b** Fe-7Ni, **c** Fe-7Ni-9Si, and **d** Fe-7Ni-15Si. Orange circles: observed Fe-Ni peaks of the B2 phase in Fe-7Ni and Fe-7Ni-9Si. Blue diamonds: observed peaks of the hcp phases in Fe-7Ni and Fe-7Ni-9Si. Red circles in **d**: observed peaks of the single B2 phase in Fe-7Ni-15Si, ×: NaCl (B2 phase, as a pressure medium), +: Re (as a gasket). Bars at the bottom of the figures show the calculated peak positions for each phase.

The nickel and silicon contents of the inner core were estimated (0–8 wt% and 3–6 wt%, respectively) based on the  $v_p$  and compression curve of the hcp Fe–6wt%Si alloy<sup>15</sup> to account for the  $v_p$  and density of the inner core of PREM<sup>16</sup>. Only the hcp phase is stable and no additional phases appeared at high pressure and temperature in the Fe–5wt%Ni–4wt%Si alloy<sup>13</sup>, and the extrapolated density of the alloy matches the density of the PREM inner core at 5800 K.

Results of the phase relations in the Fe–Ni and Fe–Ni–Si systems revealed the presence of a large stability field associated with the two-phase mixture of B2 and hcp phases under high pressure and temperature conditions. Therefore, the inner core can be considered to contain the two-phase mixture of B2 and hcp phases in the Fe–Ni–Si systems. To estimate the ratio of the two phases, we can use the EoS of the Fe–Ni and Fe–Ni–Si systems derived from this work. The details of the parameters of the EoSs are given in Table 1. The fractions of the phases can be also estimated by determining the intensities of the X-ray diffraction peaks of the B2 and hcp phases (Fig. 1). The phase relations of the Fe–Ni and Fe–Ni–Si systems given in Fig. 4 indicate that the hcp phase has a silicon content lower than that of the B2 phase.

Typical partition coefficients of silicon ( $D_{Si}$ ) between the two phases, i.e.,  $C_{B2}/C_{Hcp}$  (where  $C$  is the weight percent of silicon in each phase) at approximately 200 GPa and different temperatures are shown in Fig. 4. The  $D_{Si}$  at 1700 K is  $\sim 1.5$ , which is consistent with the previously obtained result for the Fe–9.9wt%Si alloys<sup>8</sup>. The  $D_{Si}$  increases with increasing temperature, and becomes  $\sim 20$

at 2700 K. The immiscibility gap becomes wider with increasing temperature, whereas the  $D_{Si}$  has almost no pressure dependency. Therefore, the partition coefficient  $D_{Si}$  probably becomes very large at the inner core temperature ( $\sim 6000$  K). Thus,  $D_{Si}$  at ICB conditions may be estimated to be  $>10$ .

The phase relations and the silicon partitioning between the two phases given in Fig. 4 indicate that the most reasonable composition of the two-phase mixture includes the silicon-rich B2 phase and the silicon-poor hcp phase. The density of the PREM at ICB is  $12.8 \text{ g cm}^{-3}$ <sup>16</sup>, which can be accounted for by the two-phase mixture under ICB conditions. To determine the composition of the two-phase mixture, silicon contents ( $C_{B2}$  and  $C_{Hcp}$ ) and the volume fraction of each phase are necessary. These parameters are related to the density, bulk silicon content ( $C_{Bulk}$ ), and  $D_{Si}$ , as shown in Eqs. (6)–(8) of the Methods section. Figure 5a shows reasonable combinations of the B2 (silicon rich) and hcp (silicon poor) phase mixtures for constraining the density of PREM. The silicon content in the B2 phase ( $C_{B2}$ ) and the volume fraction of the B2 phase are chosen as free parameters for constraining the density of PREM. Figure 5a shows how the B2 and hcp phases with different silicon contents should be mixed to account for the density of ICB at  $12.8 \text{ g cm}^{-3}$ <sup>16</sup>. The density and composition of each phase were calculated by using the interpolations or extrapolations from the Fe–Ni and Fe–Ni–Si EoSs obtained in this work (Table 1). Since the molar volumes of all the phases with different compositions at ICB are almost constant (Fig. 3h), the density of each phase under ICB conditions is

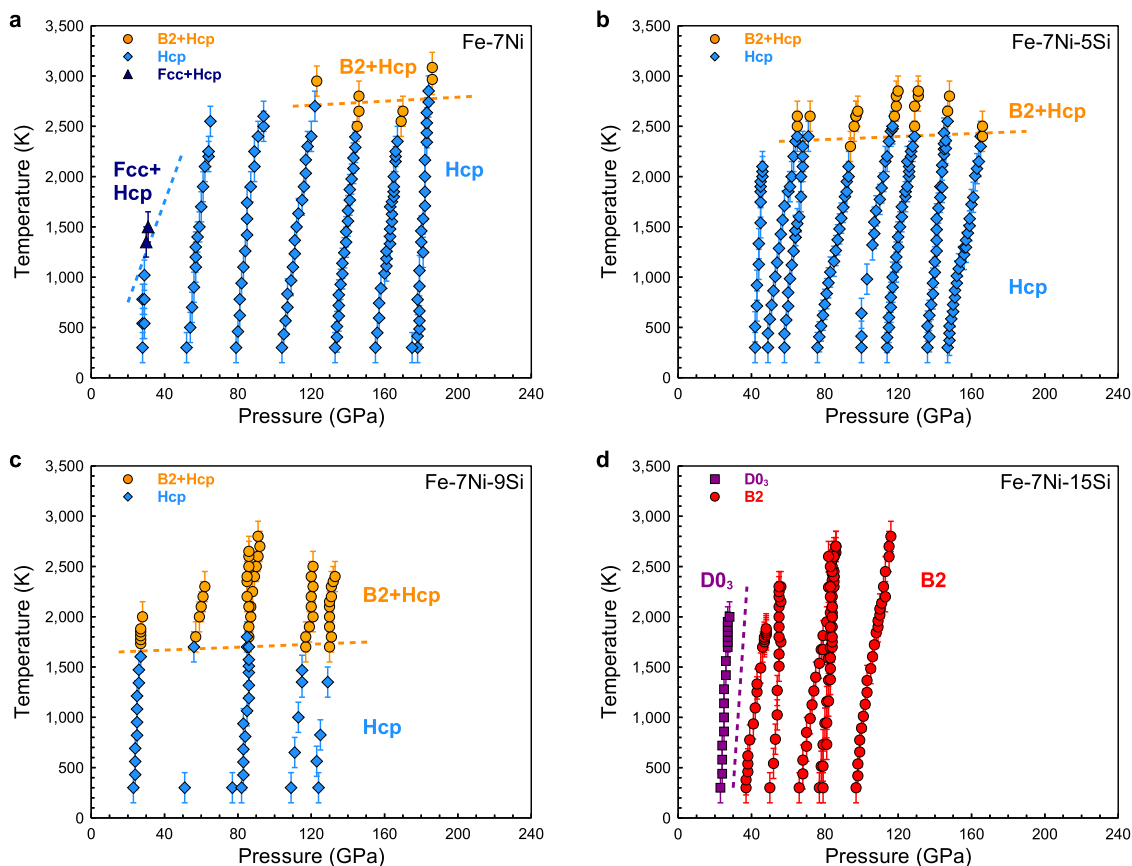


**Fig. 2** Pressure-temperature phase diagrams in the Fe-Ni/Fe-Ni-Si system. **a** Fe-7Ni, **b** Fe-7Ni-5Si, **c** Fe-7Ni-9Si, and **d** Fe-7Ni-15Si at high pressure and temperature. Pressure errors are  $\pm 2$  GPa and temperature errors are  $\pm 150$  K.

mostly dependent on its chemical composition. The detailed calculation procedure is given in the Methods section. As shown in Fig. 5a, no reasonable mixture is obtained when  $C_{\text{Bulk}}$  is less than 4 wt% (shown in black, blue, and cyan colours). The  $C_{\text{Bulk}}$  of the two-phase mixture, which can explain the density of PREM, is limited only to  $>4$  wt%; however, for  $C_{\text{Bulk}}$  to be  $\sim 4$ , it needs only a single B2 phase and not a two-phase mixture. In previous studies, two different estimations were proposed for silicon in the inner core:  $\sim 6$  wt% or higher (e.g., refs. 2,14) and  $\sim 2$  wt% or less (e.g., ref. 17). Our results support the estimation of a high silicon content ( $\sim 6$  wt%) and indicate that a low silicon content ( $\sim 2$  wt%) cannot account for the density associated with the PREM of the inner core.

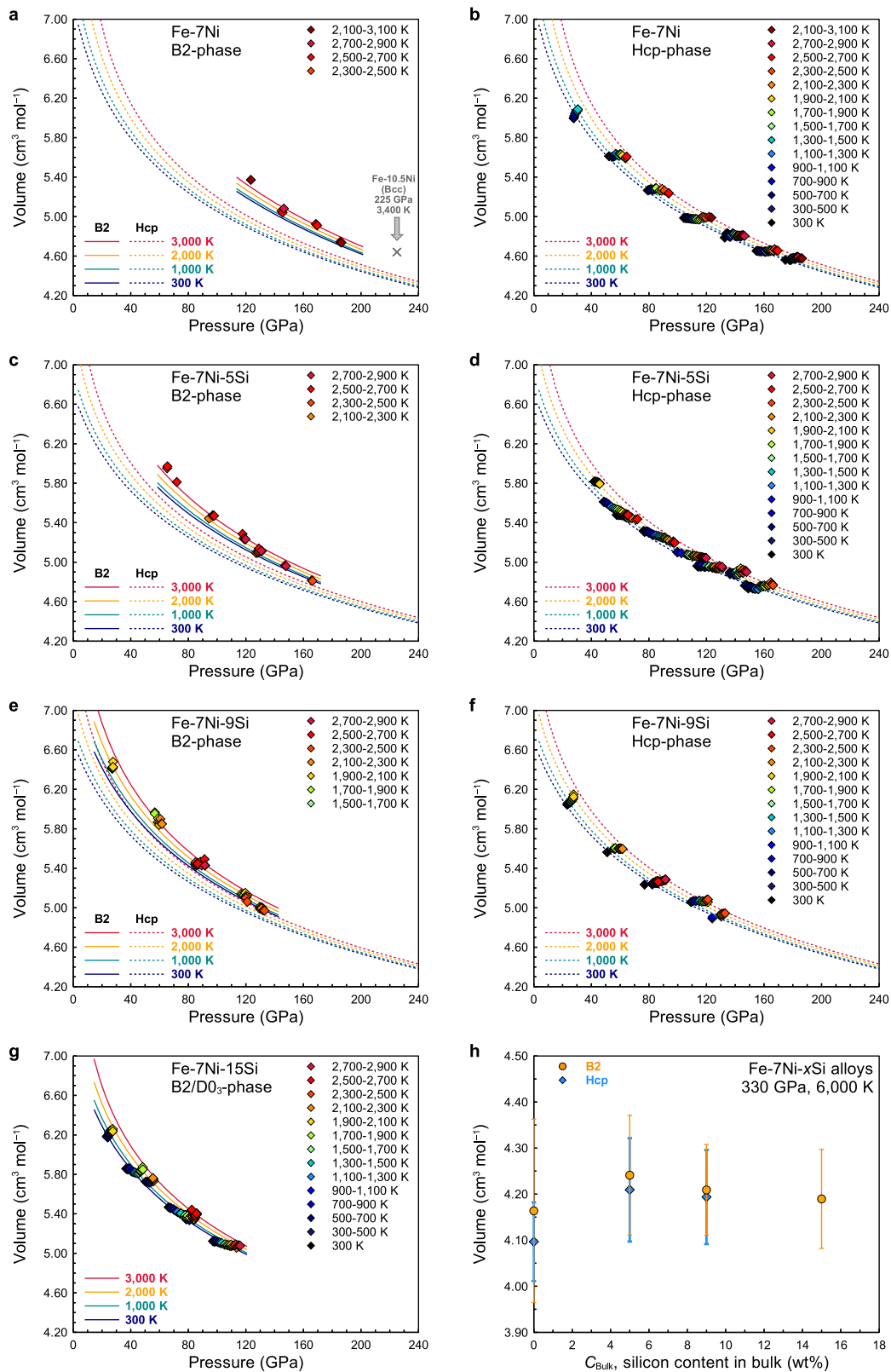
Reasonable combinations of  $C_{\text{B2}}$  and its volume fraction can be estimated as shown in Fig. 5a. The silicon content of the Earth's core was estimated to be 6 wt%<sup>2</sup> based on geochemical and cosmochemical data. The silicon content in the Earth's inner core was estimated as 6–8 wt% based on experimental studies on phase relations and EoS of the Fe–Si system at high pressure and temperature<sup>14</sup>. The  $D_{\text{Si}}$  values of coexisting B2 and hcp phases can be assumed to be  $>10$  as discussed above. Because of the uncertainty of the partition coefficient  $D_{\text{Si}}$  between B2 and hcp phases, we considered pairs of B2 and hcp phases with a large variation of  $D_{\text{Si}}$  from 10 to 75 which may cover the partition coefficient under the inner core condition and showed in Fig. 5a as black dashed lines for  $C_{\text{Bulk}}$  of 6 wt%. The silicon content of B2 and its volume fraction are shown as green, yellow, and red circles in Fig. 5a for  $D_{\text{Si}}$  values of 10, 20, and 75, respectively.

Figure 5b shows the density curves of B2 and hcp alloys at different  $D_{\text{Si}}$  values of 10, 20, and 75, the density curves of the two-phase mixture for a  $C_{\text{Bulk}}$  of 6 wt% at 6000 K, and the density

profile of the PREM of the core. For  $D_{\text{Si}}$  values between 10 to 75, the B2 phase should comprise 15–20 wt% of silicon with a volume fraction of 26–42% and the hcp phase should contain 0.2–2 wt% of silicon with a volume fraction of 58–74%. Even if  $D_{\text{Si}}$  is greater than 75, a small change in  $C_{\text{Hcp}}$  (from 0.2 wt% to almost 0 wt% silicon) does not affect the conclusion on the density and volume fraction of the two-phase mixture.

Similar density curves for  $C_{\text{Bulk}}$  values of 5 and 7 wt% are shown in Supplementary Fig. S1a, b. The  $D_{\text{Si}}$  values for the B2 and hcp alloys are not accurate in this study because the present phase boundaries exhibit certain uncertainties with regard to the weight percent, and we could not determine the compositions of the recovered products directly because of the difficulty encountered in recovering tiny samples from the sodium chloride pressure medium. However, Fig. 5 indicates that the compositional range and volume fraction of the B2 and hcp phases, which can elucidate the inner core of PREM, can be constrained by a limited combination of  $D_{\text{Si}}$  and volume fraction of the two phases.

The velocity deficits of the inner core can also be accounted for by the two-phase mixture of the B2 and hcp phases. The  $v_p$  of the PREM under ICB conditions is  $11.0 \text{ km s}^{-1}$ <sup>16</sup>, which is 6% less than that of pure iron ( $11.6 \text{ km s}^{-1}$ <sup>18</sup>). We have estimated the  $v_p$  for the two-phase mixture of the B2 and hcp phases from the present EoS and the  $v_p$  of Fe, Fe–Ni, and Fe–Si alloys under high pressure and temperature conditions<sup>15,18–22</sup>. Figure 6 shows the  $v_p$  of the B2 and hcp phases and its average value at 330 GPa and 6000 K for the two-phase mixture with a  $C_{\text{Bulk}}$  of 6 wt%, as discussed above and shown in Fig. 5b. The  $v_p$  of the B2 phase at 330 GPa and 6000 K is lower than that of the inner core at the ICB, whereas the  $v_p$  of the hcp phase is higher than that of the inner core. The averaged  $v_p$  of the two-phase mixture at 330 GPa



**Fig. 3** Volume compression and equation of state in the Fe-Ni/Fe-Ni-Si system. **a** Fe-7Ni (B2 phase), **b** Fe-7Ni (hcp phase), **c** Fe-7Ni-5Si (B2 phase), **d** Fe-7Ni-5Si (hcp phase), **e** Fe-7Ni-9Si (B2 phase), **f** Fe-7Ni-9Si (hcp phase), and **g** Fe-7Ni-15Si (B2 or DO<sub>3</sub> phase) at high pressure and temperature. x: bcc phase of Fe-10.5Ni at 225 GPa and 3400 K<sup>7</sup>. Errors are within symbols. The silicon contents of the B2 phase in the starting materials of Fe-7Ni-5Si and Fe-7Ni-9Si may be larger than these compositions. **h** The molar volumes of B2 and hcp phases with different compositions at ICB conditions. Error represents 1 $\sigma$  uncertainties.



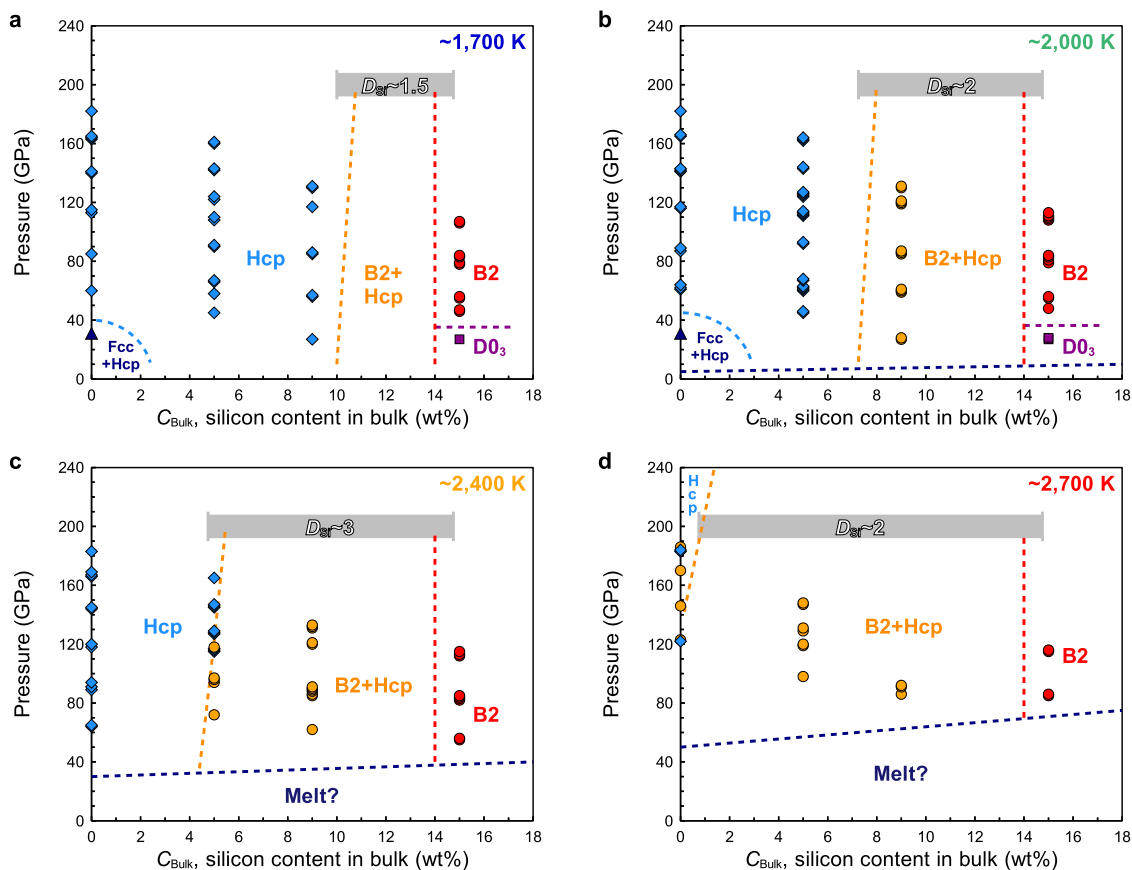


**Fig. 4** Silicon content–pressure phase diagrams in the Fe–Ni–Si system at high pressure. **a** ~1700 K, **b** ~2000 K, **c** ~2400 K, and **d** ~2700 K. The dashed lines indicate presumable phase transition boundaries estimated by the fraction of the two phases based on X-ray peak intensities. The pressure–temperature phase boundaries are shown in Fig. 2. The grey bars represent the typical partition coefficients of silicon ( $D_{Si}$ ) (i.e., the ratios of silicon contents of the B2 ( $C_{B2}$ ) and the hcp ( $C_{Hcp}$ ) phases at 200 GPa. Errors are within symbols.

**Table 1** Parameters of the equation of state for hexagonal close-packed (hcp) and ordered derivatives of body-centred cubic (B2/ $DO_3$ ) phases in Fe–Ni–Si alloys.

Bulk composition	Phase	$V_0$ ( $\text{cm}^3 \text{mol}^{-1}$ )	$K_0$ (GPa)	$K_0'$	$\theta_0$ (K)	$\gamma_0$	$q$
Fe–7Ni	hcp	7.183 (0.106)	93 (4)	6.68 (0.10)	777 (223)	1.80 (0.17)	1 (fixed) <sup>§</sup>
Fe–7Ni–5Si	hcp	6.724 (0.141)	147 (12)	6.65 (0.24)	777 (fixed) <sup>†</sup>	1.67 (0.14)	1 (fixed) <sup>§</sup>
Fe–7Ni–9Si	hcp	6.685 (0.148)	161 (8)	6.30 (0.19)	777 (fixed) <sup>†</sup>	1.51 (0.15)	1 (fixed) <sup>§</sup>
Fe–7Ni	B2	7.583 (0.336)	138 (16)	4.61 (0.39)	968 (fixed) <sup>††</sup>	1.80 (fixed) <sup>‡</sup>	1 (fixed) <sup>§</sup>
Fe–7Ni–5Si*	B2	7.274 (0.162)	131 (11)	5.74 (0.30)	968 (fixed) <sup>††</sup>	1.67 (fixed) <sup>‡‡</sup>	1 (fixed) <sup>§</sup>
Fe–7Ni–9Si*	B2	7.154 (0.109)	131 (7)	5.95 (0.19)	968 (fixed) <sup>††</sup>	1.51 (fixed) <sup>‡‡‡</sup>	1 (fixed) <sup>§</sup>
Fe–7Ni–15Si	B2/ $DO_3$	7.126 (0.098)	106 (7)	6.86 (0.34)	968 (265)	1.33 (0.13)	1 (fixed) <sup>§</sup>

Note:

$V$  is molar volume,  $K$  and  $K'$  are isothermal bulk modulus and its first pressure derivative,  $\theta$  is Debye temperature,  $\gamma$  and  $q$  are Grüneisen parameter and its volume dependence, and the subscript zero refers to ambient conditions. The thermoelastic parameters of hcp Fe–7Ni and those of B2/ $DO_3$  Fe–7Ni or Fe–7Ni–15Si are determined from our data. The partial parameters for the different compositions are fixed to those for the measured values for hcp and B2/ $DO_3$  phases.

\*Silicon contents of B2 alloys may be larger than that of the bulk compositions.

<sup>†</sup>Fixed to the value of hcp Fe–7Ni. <sup>††</sup>Fixed to the value of B2 Fe–7Ni–15Si.

<sup>‡</sup>Fixed to the value of hcp Fe–7Ni. <sup>‡‡</sup>Fixed to the value of hcp Fe–7Ni–5Si. <sup>‡‡‡</sup>Fixed to the value of hcp Fe–7Ni–9Si.

<sup>§</sup>Fixed to 1.

and 6000 K is  $10.95 \pm 0.50 \text{ km s}^{-1}$ . For an inner core with a  $C_{\text{Bulk}}$  of 5 or 7 wt%, the averaged  $v_p$  is shown in Supplementary Fig. S1c, d. For a  $C_{\text{Bulk}}$  of 5 and 7 wt%, the averaged  $v_p$  slightly deviates from that of PREM (the  $C_{\text{Bulk}}$  of 6), but it is within the error range. Although the  $v_p$  of the two-phase mixture is not accurate enough to constrain the light element content in the core due to a lack of suitable wave velocity data for Fe–Ni–Si alloys under high pressure and temperature conditions, the averaged  $v_p$  for the two-phase mixture at 330 GPa and 6000 K is consistent

with that of the inner core of PREM at ICB. The detailed procedure for the estimation of the  $v_p$  is given in the Methods section. Therefore, the existence of the B2 phase can elucidate the properties of the inner core, such as its deficits in terms of density and  $v_p$ , although further experiments under high pressure and temperature conditions are necessary to unambiguously constrain the composition of the core.

A simple model of the single hcp phase of Fe–Ni–Si alloy cannot account for several enigmatic properties of the inner core

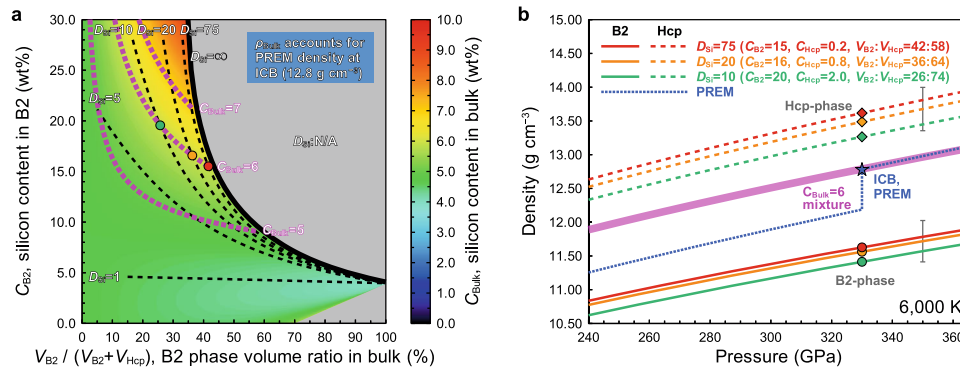


**Fig. 5 Silicon content, volume ratio, and pressure-density relationship of two-phase mixtures of B2 and hcp phases to account for the PREM density.** **a** Reasonable silicon content in the bulk composition of the two-phase mixture of B2 and hcp phases to account for the density of the PREM at the ICB condition of  $12.8 \text{ g cm}^{-3}$ . Horizontal and vertical axes represent the volume ratio of the B2 phase and the silicon content of the B2 phase ( $C_{B2}$ ), respectively. Silicon content of the hcp phase ( $C_{Hcp}$ ) (not described in this figure) is constrained by the PREM density with Eqs. (6)–(8).  $C_{Bulk}$  values are  $>4 \text{ wt}\%$  as shown in the colour contour (silicon contents of  $<4 \text{ wt}\%$  are not available, which are shown by black, blue, and cyan colours). The  $C_{B2}$  and volume ratio of B2 phase in the grey areas cannot reproduce the density of the PREM inner core. Variations of  $D_{Si}$  (i.e.,  $C_{B2}/C_{Hcp}$ ) of 1, 5, 10, 20, and 75 are shown as black dashed curves.  $D_{Si}$  of  $\infty$  (which means  $C_{Hcp}$  is almost 0 wt%) is shown as a black bold curve. The curves of  $D_{Si} = 75$  and  $\infty$  are close, which indicates that the compositions and volume fraction of the two-phase pairs for  $D_{Si} = 75$  and  $\infty$  are almost the same. Typical  $C_{Bulk}$  of 5, 6, and 7 wt% are shown as magenta dotted lines. Colour circles represent typical conditions for  $C_{Bulk} = 6$  with  $D_{Si} = 75$  (red),  $D_{Si} = 20$  (orange), and  $D_{Si} = 10$  (green). **b** Pressure-density relations at  $C_{Bulk} = 6$  and B2 and hcp phases at 6000 K.  $C_{B2}$  and  $C_{Hcp}$  and volume percent ratios of  $V_{B2}$  and  $V_{Hcp}$  corresponding to the conditions in Fig. 5a are shown. Grey bars represent  $1\sigma$  error of the EoS. The discontinuity of the blue dotted line represents the boundary of the liquid outer core and the solid inner core of PREM. Blue star represents the inner core of PREM at ICB. Coloured diamonds with dashed curves represent the density of the hcp phase at ICB and density curve at high pressure and 6000 K. Coloured circles are of the B2 phase. Pairs of the same colour symbols can account for the PREM density at ICB (a blue star). Magenta line represents the combined EoS of the two-phase mixture of the B2 and hcp phases. The density curves of the three models of the two-phase mixtures are within the width of the line.

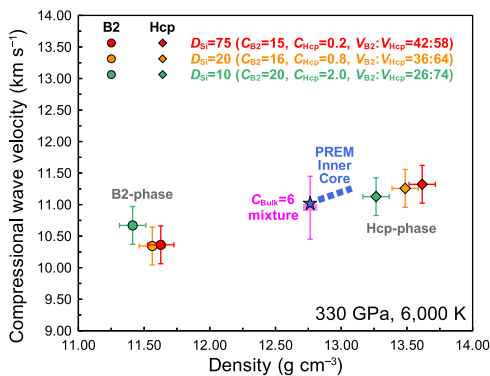


**Fig. 6 Compressional wave velocity for the two-phase mixture of the B2 and hcp phases for a bulk silicon content of 6 wt% ( $C_{Bulk} = 6$ ) at 330 GPa and 6000 K.** A magenta rectangular symbol represents the averaged velocity (see Methods section) of the three models for two-phase mixtures shown in Fig. 5b. Symbols are same as those in Fig. 5b. The error bars represent  $1\sigma$  error.

such as the anomalously low shear wave velocity and the high Poisson ratio, despite consistencies observed in terms of composition and density of the inner core<sup>23</sup>. To account for such properties of the inner core, the existence of a pre-melting effect observed in the pure iron hcp phase has been suggested<sup>24</sup>. However, since the absence of this effect was reported in the Fe–Si alloy<sup>25</sup>, a better explanation is required for the existence of such properties of the inner core.

The physical properties of the B2 phase are considered similar to those of the bcc phase, as the B2 structure has an ordered arrangement of nickel and silicon atoms in the bcc lattice. The possible existence of the bcc phase in the inner core has been suggested by theoretical calculations<sup>6,26</sup>. These theoretical studies imply that the bcc phase may be stable at a particularly narrow temperature range just below the melting temperature and may

show noticeable shear softening. Our observations of the Fe–Ni–Si alloy and those for Fe–10.5Ni<sup>7</sup> reveal the existence of a bcc phase and/or its ordered derivative phase at high pressures and temperatures, which is consistent with ab initio calculations<sup>6,26</sup>.

The low viscosity of the bcc phase of iron under inner core conditions reported recently<sup>27</sup> may be consistent with the properties of the inner core<sup>23</sup>. The present experiments and these theoretical calculations indicate that the coexistence of the B2 and hcp phases in the Fe–Ni–Si alloy may account for the enigmatic properties in the inner core. A high seismic attenuation and shear softening associated with the bcc–fcc (face-centred cubic) transition of iron at high temperatures was observed with using low-frequency resonance measurements<sup>28</sup>. This relaxation may be caused by the reversible climb and glide of dislocations in sub-grain boundaries and/or reversible grain boundary migration associated with the diffusion process<sup>28</sup>. Similar phenomena might be expected in the transformation of the bcc phase into the hcp phase in the inner core. The phase transition between bcc and hcp is called the martensitic transition, during which crystallographic relationships are observed between the two phases. Shear softening associated with the martensitic transition of a bcc structure to its hcp counterpart has been reported in several metal alloys<sup>29,30</sup>. Therefore, the mechanical interaction of the coexisting pair of B2 and hcp phases in Fe–Ni–Si alloys may also account for the properties of the inner core with its low shear wave velocity and low viscosity.

## Methods

**Starting material.** The starting materials used in this study include homogeneous iron, nickel, and silicon alloys with four different compositions, which were synthesised via rapid quenching (about a few seconds) after melting of the starting powdered mixtures with the yttrium aluminium garnet laser in an argon atmosphere. The powdered mixtures were made by mixing iron (99.9% purity; Wako), nickel (99.9% purity; Wako), and silicon (99.9% purity; Wako) reagents, which were ground in an agate mortar to homogenise the mixtures. The four starting compositions were Fe–7Ni (7 wt% nickel), Fe–7Ni–5Si (7 wt% nickel and 5 wt%

silicon), Fe–7Ni–9Si (7 wt% nickel and 9 wt% silicon), and Fe–7Ni–15Si (7 wt% nickel and 15 wt% silicon); these compositions can also be represented as  $\text{Fe}_{(0.94-x)}\text{Ni}_{0.06}\text{Si}_x$  ( $x = 0, 0.09, 0.16, 0.26$ ; where  $x$  represents the atomic fraction). The compositions of samples were confirmed using electron probe micro-analyser measurements. Heterogeneity in iron, nickel, and silicon compositions of four starting materials were all within 1 wt%, which was confirmed using a field emission scanning electron microscope (FE-SEM, JEOL). Typical examples of backscattered electron images are given in Supplementary Fig. S2, which show mosaic texture probably due to rapid quenching, but there were no differences in composition.

**High pressure and temperature X-ray diffraction measurements.** To generate high pressures, depending on the experimental pressures, we used a diamond anvil cell with bevelled diamond anvils that exhibit culet diameters of 75, 100, and 150  $\mu\text{m}$ . A sample foil with a thickness of approximately 20  $\mu\text{m}$  was sandwiched between sodium chloride pellets of <5  $\mu\text{m}$  thickness; this foil served as the pressure medium, thermal insulator, and pressure marker. The sample was loaded into a sample hole of a pre-compressed rhenium gasket (99.9%; Alfa Aesar), which was typically about 20–30  $\mu\text{m}$  in thickness. In-situ high pressure and temperature experiments were conducted using BL10XU of SPring-8<sup>31</sup>. We used a monochromatic X-ray beam with a typical wavelength of  $0.4136 \pm 0.003 \text{ \AA}$  that was collimated to a diameter of 10  $\mu\text{m}$ . The sample was heated using the double-sided laser heating method<sup>31</sup> by employing a fibre laser at BL10XU of SPring-8. The laser heating area (20  $\mu\text{m}$  in diameter) was adequately large compared to the size of the X-ray beam to reduce the effect of the temperature gradient for the phase observations. We checked the X-ray position using the X-ray fluorescence of diamonds before heating. Therefore, the X-ray and heating areas were aligned well. Temperature measurements were made by using the spectrographic method, in which the radiation from the heated sample was used for the determination of temperatures above 1600–1700 K; temperatures below 1600–1700 K were estimated using the laser power–temperature relations in high temperature conditions. The temperature measurements were performed for several tens of seconds during heating. The maximum temperature uncertainties during heating at a constant temperature were within  $\pm 150 \text{ K}$  including the uncertainty due to the heating system, the temperature differences between the two heated sides, and temperature fluctuations during heating. The temperature uncertainty at low temperature was estimated from the laser power–temperature relation at high temperatures was estimated to be the same, although it might be smaller than  $\pm 150 \text{ K}$ . The experimental pressure was determined based on the lattice parameters of sodium chloride using the EoSs of the B1<sup>32</sup> and B2 phases<sup>33</sup>. The temperature distribution in the pressure medium, which was heated by the double-sided laser heating diamond anvil cell, has been evaluated based on three-dimensional numerical modelling<sup>34</sup>. These model calculations indicated that the temperature difference between the centre and anvil surfaces in the sodium chloride pressure medium (with a thickness of 1–2  $\mu\text{m}$ ) was approximately 100–200 K at 2000 K; this value was equivalent to the temperature uncertainty in this experiment. The error associated with pressure ( $\pm 2 \text{ GPa}$ ) was evaluated using the errors observed in the volume of sodium chloride and the standard deviation of the temperature fluctuations. A flat-panel detector (FPD: Perkin Elmer XRD0822,  $1024 \times 1024$  pixels, 200  $\mu\text{m}$  per pixel, CsI deposited type, with 16-bit dynamic range) was used as an X-ray detector because it was important to capture diffraction patterns within a short duration of time. The typical exposure time for obtaining diffraction patterns was 2 s per 1 shot; this was repeated 20 times, and data were averaged for each pattern. The samples were compressed to a certain pressure at an ambient temperature and then subjected to increasing temperatures. The X-ray diffraction patterns in the samples were recorded at ambient temperatures, while the temperature was increased in steps from 50–100 K under high temperature conditions at each pressure (depending on laser power currents). Stable coexistence of the B2 and hcp phases under high pressure and temperature conditions was detected based on the appearance of the diffraction peaks associated with the B2 phase at high temperatures in the Fe–7Ni/Fe–7Ni–5Si/Fe–7Ni–9Si system. The diffraction patterns were analysed using the IPAnalyzer and PDIndexer software packages<sup>35</sup>, with peak fitting being conducted using symmetric pseudo-Voigt functions. The phase and its unit cell parameters were identified by the peak positions.

**Thermal equation of state of Fe–Ni and Fe–Ni–Si alloys.** The experimental pressure–volume ( $P$ - $V$ ) compression data for Fe–Ni and Fe–Ni–Si alloys at ambient temperature were fitted using the Rydberg–Vinet EoS<sup>36</sup> as follows:

$$P_{(V,300\text{K})} = 3K_0 \left( \frac{V}{V_0} \right)^{-\frac{2}{3}} \left[ 1 - \left( \frac{V}{V_0} \right)^{\frac{1}{3}} \right] \exp \left\{ \frac{3}{2} (K'_0 - 1) \left[ 1 - \left( \frac{V}{V_0} \right)^{\frac{1}{3}} \right] \right\}, \quad (1)$$

where  $K$ ,  $K'$ , and  $V$  are the isothermal bulk modulus, its first pressure derivative, and the molar volume, respectively; the subscript zero refers to ambient conditions. The total pressure at high temperatures was expressed by the Mie–Grüneisen–Debye model (e.g., ref. 37) as follows:

$$P_{(V,T)} = P_{(V,300\text{K})} + [P_{\text{th}(V,T)} - P_{\text{th}(V,300\text{K})}] \quad (2)$$

where the thermal pressure  $P_{\text{th}}$  is derived as follows:

$$P_{\text{th}(V,T)} = 9nRT \frac{\gamma}{V} \left( \frac{T}{\Theta} \right)^3 \int_0^{\Theta/T} \frac{x^3}{e^x - 1} dx \quad (3)$$

where  $n$  is the number of atoms per chemical formula unit,  $R$  is the gas constant,  $\gamma$  is the Grüneisen parameter,  $T$  is the temperature, and  $\Theta$  is the Debye temperature. The Grüneisen parameter and the Debye temperature are usually expressed as a function of volume with a negligible temperature dependence<sup>38</sup> as follows:

$$\gamma = \gamma_0 \left( \frac{V}{V_0} \right)^q, \quad (4)$$

$$\Theta = \Theta_0 \exp \left( \frac{\gamma_0 - \gamma}{q} \right), \quad (5)$$

where  $q$  is the volume dependence on the Grüneisen parameter.

**Estimation of the density of the two-phase mixture of the B2 and hcp phases.** Bulk silicon contents of the two-phase mixture and the volume ratio of the B2 and hcp phases, which account for the density of PREM (12.8  $\text{g cm}^{-3}$ )<sup>16</sup> under ICB conditions, are shown in Fig. 5a. The density of each phase and composition under ICB conditions were determined using experimental EoSs (Table 1) and the following constraints:

$$\rho_{\text{Bulk}} = x\rho_{\text{B2}(C_{\text{B2}})} + (1-x)\rho_{\text{Hcp}(C_{\text{Hcp}})}, \quad (6)$$

The bulk silicon content can be expressed by the following relation:

$$C_{\text{Bulk}}\rho_{\text{Bulk}} = C_{\text{B2}}x\rho_{\text{B2}(C_{\text{B2}})} + C_{\text{Hcp}}(1-x)\rho_{\text{Hcp}(C_{\text{Hcp}})}, \quad (7)$$

$$D_{\text{Si}} = C_{\text{B2}}/C_{\text{Hcp}}, \quad (8)$$

where  $x$  is the volume fraction of the B2 phase,  $x = \frac{V_{\text{B2}}}{V_{\text{B2}} + V_{\text{Hcp}}}$ ,  $\rho_{\text{B2}(C_{\text{B2}})}$  and  $\rho_{\text{Hcp}(C_{\text{Hcp}})}$  are the densities of the B2 and hcp phases, respectively, for compositions coexisting under ICB conditions derived from the  $D_{\text{Si}}$ .

Three parameters ( $C_{\text{B2}}$ ,  $C_{\text{Hcp}}$ , and  $x$ ) in Eqs. (6)–(8) should be specified to determine the density of the two-phase mixture. The parameters  $\rho_{\text{B2}(C_{\text{B2}})}$  and  $\rho_{\text{Hcp}(C_{\text{Hcp}})}$  indicate the densities of the B2 and hcp phases that coexist under ICB conditions and are derived from the molar volume of the phase ( $V_{\text{Phase}}$ ) and the molecular weight ( $M_{\text{Phase}}$ ) of the alloys:

$$\rho_{\text{Phase}(C_{\text{Phase}})} = \frac{M_{\text{Phase}}}{V_{\text{Phase}}}, \quad (9)$$

where  $M_{\text{Phase}}$  is the molecular weight of the Fe–Ni–Si alloys and  $V_{\text{Phase}}$  is its molar volume under ICB conditions for each phase.

The silicon-rich B2 phase and the silicon-poor hcp phase are reasonable combinations of the two-phase mixture (Fig. 4 and refs. 8,11). The EoSs of the silicon rich B2 phases were estimated based on the EoS of a single phase of B2 in the Fe–7Ni–15Si alloy and that of the B2 phase of Fe–7Ni. The EoSs of the silicon-poor hcp phases were estimated based on the EoS of a single hcp phase observed at lower temperatures in the Fe–Ni–Si system (see Fig. 2). The parameters of the EoSs for hcp and B2/D0<sub>3</sub> phases have been experimentally determined and are given in Table 1. The molar volumes of the two phases under ICB conditions (Fig. 3h) show constant values with almost no compositional dependency. The densities of the coexisting pair of the B2 and hcp phases,  $\rho_{\text{B2}(C_{\text{B2}})}$  and  $\rho_{\text{Hcp}(C_{\text{Hcp}})}$ , are derived from the constant molar volume of the two phases at ICB as shown in Fig. 3h. Therefore, the ambiguity of the density associated with the uncertainty of the silicon contents in the two phases may not have large impacts on our discussions that consider the density constraints with respect to the PREM.

**Compressional wave velocity for Fe–Ni and Fe–Ni–Si alloys and the estimation of the average compressional wave velocity of the two-phase mixture.** Owing to the lack of suitable data for the wave velocities of Fe–Ni–Si alloys, the  $v_p$  of Fe–Ni–Si alloys was estimated by the silicon and nickel dependency of  $v_p$  in Fe–Si<sup>15,18,19,21,22</sup> and Fe–Ni alloys<sup>20</sup>.

The average  $v_p$  of the two-phase assemblage shown in Fig. 6 was calculated as follows: the  $v_p$  for hcp and B2 Fe–Si alloys with various silicon contents were estimated based on the density–velocity systematics (known as Birch's law<sup>39</sup>) by using the  $v_p$  calculated at a high pressure and an ambient temperature for the hcp phases of Fe<sup>18</sup>, Fe–5wt%Si<sup>21</sup>, Fe–6wt%Si<sup>15</sup>, and Fe–9wt%Si<sup>19</sup>, and the bcc/B2 phase of Fe–10wt%Si, Fe–15wt%Si, Fe–19wt%Si, Fe–21wt%Si, and Fe–29wt%Si<sup>22</sup>. The effect of 7 wt% nickel in the alloys was estimated from the  $v_p$  of hcp-Fe<sup>18</sup> and the hcp-alloys of Fe–5wt%Ni and Fe–15wt%Ni<sup>20</sup>. The  $v_p$  of Fe–5wt%Ni and Fe–15wt%Ni is  $\sim 3\%$  and  $\sim 6\%$  smaller than that of non-nickel alloys, respectively, with almost no density dependence within the error ranges<sup>18,20</sup>. By combining the estimated  $v_p$  that includes the effect of silicon and nickel, the  $v_p$  of Fe–Ni–Si alloys at a high pressure and an ambient temperature was estimated to be a linear function of density as follows:

$$v_{p(\text{Fe–zSi})}(\rho, 300 \text{ K}) = A_z\rho - B_z, \quad (10)$$



$$v_{p(\text{Fe}-y\text{Ni}-z\text{Si})}(\rho, 300\text{ K}) = N_y v_{p(\text{Fe}-z\text{Si})}(\rho, 300\text{ K}), \quad (11)$$

where  $A_z$  and  $B_z$  are the parameters associated with the Birch's law of Fe–Si alloys including  $z$  wt% silicon, which was interpolated from the Birch's law of Fe and Fe–Si alloys<sup>15,18,19,21,22</sup>.  $N_y$  is the coefficient that represents the effect of including  $y$  wt% nickel in the alloys. Here, we used  $N_y = 0.96 (\pm 0.01)$  for alloys with 7 wt% nickel, which was estimated from the  $v_p$  of hcp-Fe<sup>18</sup>, Fe–5wt%Ni, and Fe–15wt% Ni<sup>20</sup>. High-temperature velocity was estimated by using the temperature dependence of the Birch's law<sup>15,18</sup>. The temperature dependence of  $v_p$  for Fe–Ni–Si alloys was assumed to be the same as that of Fe–6wt%Si<sup>15</sup>. The average  $v_p$  of the two-phase mixture was calculated using the mean of the arithmetic and harmonic means of the elastic modulus ( $K_S + \frac{4}{3}G = \rho v_p^2$ ), which is termed as the Voigt–Reuss–Hill average of the elastic constants of the composite material (e.g., ref. 40). The elastic modulus is proportional to  $\rho v_p^2$ ; consequently, the average  $v_p$  of the two-phase mixture can be estimated as follows:

$$B_{\text{arith}} = x\rho_{\text{B2}}v_{p(\text{B2})}^2 + (1-x)\rho_{\text{Hcp}}v_{p(\text{Hcp})}^2, \quad (12)$$

$$B_{\text{harm}} = 1/\left[\frac{x}{\rho_{\text{B2}}v_{p(\text{B2})}^2} + \frac{1-x}{\rho_{\text{Hcp}}v_{p(\text{Hcp})}^2}\right], \quad (13)$$

$$\rho_{\text{Bulk}}v_{p(\text{Bulk})}^2 = \frac{1}{2}(B_{\text{arith}} + B_{\text{harm}}). \quad (14)$$

where  $x$  is the volume fraction of the B2 phase, which is expressed as  $x = \frac{V_{\text{B2}}}{V_{\text{B2}} + V_{\text{Hcp}}}$ .

## Data availability

All data used in this study are presented in the text and supplementary information. Parameters used in the calculation are described in the Methods section and Table 1. The data used to produce Figs. 1–6 and Supplementary Fig. S1 and additional Supplementary Data can be accessed from the public repository Zenodo (<https://doi.org/10.5281/zenodo.5527625>).

Received: 30 May 2021; Accepted: 6 October 2021;

Published online: 28 October 2021

## References

- Goldstein, J. I., Scott, E. R. D. & Chabot, N. L. Iron meteorites: crystallization, thermal history, parent bodies, and origin. *Chemie der Erde* **69**, 293–325 (2009).
- McDonough, W. F. Compositional model for the Earth's core. In *Treatise on Geochemistry 2nd Edition Vol. 3: The Mantle and Core* (eds Holland H. D. & Turekian K. K.). 559–577 (Elsevier, 2014). <https://doi.org/10.1016/B978-0-08-095975-7.00215-1>.
- Dewaale, A. et al. Quasihydrostatic equation of state of iron above 2 Mbar. *Phys. Rev. Lett.* **97**, 215504 (2006).
- Sakai, T. et al. Equation of state of pure iron and Fe<sub>0.9</sub>Ni<sub>0.1</sub> alloy up to 3 Mbar. *Phys. Earth Planet. Inter.* **228**, 114–126 (2014).
- Ringwood, A. E. On the chemical evolution and densities of the planets. *Geochim. Cosmochim. Acta.* **15**, 257–283 (1959).
- Belonoshko, A. B., Ahuja, R. & Johansson, B. Stability of the body-centred-cubic phase of iron in the Earth's inner core. *Nature* **424**, 1032–1034 (2003).
- Dubrovinsky, L. S. et al. Body-centered cubic iron–nickel alloy in Earth's core. *Science* **316**, 1880–1883 (2007).
- Kuwayama, Y., Sawai, T., Hirose, K., Sata, N. & Ohishi, Y. Phase relations of iron–silicon alloys at high pressure and high temperature. *Phys. Chem. Miner.* **36**, 511–518 (2009).
- Lin, J. F. Phase relations of Fe–Si alloy in Earth's core. *Geophys. Res. Lett.* **36**, L06306 (2009).
- Fischer, R. A. et al. Phase relations in the Fe–FeSi system at high pressures and temperatures. *Earth Planet. Sci. Lett.* **373**, 54–64 (2013).
- Fischer, R. A. & Campbell, A. J. The axial ratio of hcp Fe and Fe–Ni–Si alloys to the conditions of Earth's inner core. *Am. Mineral.* **100**, 2718–2724 (2015).
- Tateno, S., Kuwayama, Y., Hirose, K. & Ohishi, Y. The structure of Fe–Si alloy in Earth's inner core. *Earth Planet. Sci. Lett.* **418**, 11–19 (2015).
- Komabayashi, T. et al. Phase relations in the system Fe–Ni–Si to 200 GPa and 3900 K and implications for Earth's core. *Earth Planet. Sci. Lett.* **512**, 83–88 (2019).
- Fischer, R. A. et al. Equations of state in the Fe–FeSi system at high pressures and temperatures. *J. Geophys. Res.* **119**, 2810–2827 (2014).
- Sakairi, T. et al. Sound velocity measurements of hcp Fe–Si alloy at high pressure and high temperature by inelastic x-ray scattering. *Am. Mineral.* **103**, 85–90 (2018).
- Dziewonski, A. M. & Anderson, D. L. Preliminary reference Earth model. *Phys. Earth Planet. Inter.* **25**, 297–356 (1981).
- Antonangeli, D. et al. Composition of the Earth's inner core from high-pressure sound velocity measurements in Fe–Ni–Si alloys. *Earth Planet. Sci. Lett.* **295**, 292–296 (2010).
- Sakamaki, T. et al. Constraints on Earth's inner core composition inferred from measurements of the sound velocity of hcp-iron in extreme conditions. *Sci. Adv.* **2**, e1500802 (2016).
- Antonangeli, D. et al. Sound velocities and density measurements of solid hcp-Fe and hcp-Fe–Si (9 wt.%) alloy at high pressure: constraints on the Si abundance in the Earth's inner core. *Earth Planet. Sci. Lett.* **482**, 446–453 (2018).
- Wakamatsu, T., Ohta, K., Yagi, T., Hirose, K. & Ohishi, Y. Measurements of sound velocity in iron–nickel alloys by femtosecond laser pulses in a diamond anvil cell. *Phys. Chem. Miner. B* **45**, 589–595 (2018).
- Edmund, E. et al. Velocity-density systematics of Fe–5wt%Si: constraints on Si content in the Earth's inner core. *J. Geophys. Res.* **124**, 3436–3447 (2019).
- Edmund, E. et al. Structure and elasticity of cubic Fe–Si alloys at high pressures. *Phys. Rev. B* **100**, 134105 (2019).
- Deuss, A. Heterogeneity and anisotropy of Earth's inner core. *Annu. Rev. Earth Planet. Sci.* **42**, 103–126 (2014).
- Martorell, B., Vocadlo, L., Brodholt, J. & Wood, I. G. Strong premelting effect in the elastic properties of hcp-Fe under inner-core conditions. *Science* **342**, 466–468 (2013).
- Martorell, B., Wood, I. G., Brodholt, J. & Vocadlo, L. The elastic properties of hcp-Fe<sub>1-x</sub>Si<sub>x</sub> at Earth's inner-core conditions. *Earth Planet. Sci. Lett.* **451**, 89–96 (2016).
- Vocadlo, L. et al. Possible thermal and chemical stabilization of body-centred-cubic iron in the Earth's core. *Nature* **424**, 536–539 (2003).
- Belonoshko, A. B., Fu, J., Bryk, T., Simak, S. I. & Mattesini, M. Low viscosity of the Earth's inner core. *Nat. Commun.* **10**, 2483 (2019).
- Jackson, I., Fitz Gerald, J. D. & Kokkonen, H. High-temperature viscoelastic relaxation in iron and its implications for the shear modulus and attenuation of the Earth's inner core. *J. Geophys. Res.* **105**, 23605–23634 (2000).
- Ding, X. et al. Experimental study of elastic constant softening prior to stress-induced martensitic transformation. *Phys. Rev. B* **77**, 174103 (2008).
- Ren, X. et al. Elastic constants of Ti<sub>50</sub>Ni<sub>30</sub>Cu<sub>20</sub> alloy prior to martensitic transformation. *Philos. Mag. A* **79**, 31–41 (1999).
- Hirao, N. et al. New developments in high-pressure x-ray diffraction beamline for diamond anvil cell at SPring-8. *Matter Radiat. Extreme* **5**, 018403 (2020).
- Brown, J. M. The NaCl pressure standard. *J. Appl. Phys.* **86**, 5801–5808 (1999).
- Ueda, Y., Matsui, M., Yokoyama, A., Tange, Y. & Funakoshi, K. Temperature-pressure-volume equation of state of the phase of sodium chloride. *J. Appl. Phys.* **103**, 113513 (2008).
- Rainey, E. S. G., Hernlund, J. W. & Kavner, A. Temperature distributions in the laser-heated diamond anvil cell from 3-D numerical modeling. *J. Appl. Phys.* **114**, 204905 (2013).
- Seto, Y., Nishio-Hamane, D., Nagai, T. & Sata, N. Development of a software suite on x-ray diffraction experiments. *Rev. High Press. Sci. Technol.* **20**, 269–276 (2010).
- Vinet, P., Rose, J. H., Ferrante, J. & Smith, J. R. Universal features of the equation of state of solids. *J. Phys. Condens. Matter* **1**, 1941–1963 (1989).
- Poirier, J. P. *Introduction to the Physics of the Earth's Interior* 2nd edn (Cambridge Univ. Press, 2000). <https://doi.org/10.1017/CBO9781139164467>.
- Anderson, O. L. *Equations of State of Solids for Geophysics and Ceramic Science* (Oxford Univ. Press, 1995). <https://global.oup.com/academic/product/9780195056068>.
- Birch, F. The velocity of compressional waves in rocks to 10 kilobars: 1. *J. Geophys. Res.* **65**, 1083–1102 (1960).
- Hill, R. The elastic behaviour of a crystalline aggregate. *Proc. Phys. Soc. A* **65**, 349–354 (1952).

## Acknowledgements

This study was supported by the JSPS KAKENHI Grant Number JP15H05748 and JP20H00187 to E. Ohtani. The synchrotron X-ray experiments were performed at the BL10XU of SPring-8 with the approval of the Japan Synchrotron Radiation Research Institute (JASRI) (Proposal Nos. 2017B1514, 2018A1447, and 2018B1500). We thank S. I. Kawaguchi for her assistance with the XRD experiments and S. Ozawa and Y. Ito for their assistance with composition analysis of the starting materials.

## Author contributions

E. Ohtani devised the project. D. Ikuta performed the sample preparation and managed the experimental plan. D. Ikuta, E. Ohtani, and N. Hirao participated in the experiments. D. Ikuta analysed the data. D. Ikuta and E. Ohtani wrote the manuscript with inputs from N. Hirao.

## Competing interests

The authors declare no competing interests.

**Additional information**

**Supplementary information** The online version contains supplementary material available at <https://doi.org/10.1038/s43247-021-00298-1>.

**Correspondence** and requests for materials should be addressed to Daijo Ikuta or Eiji Ohtani.

**Peer review information** *Communications Earth & Environment* thanks Renbiao Tao and Yigang Zhang for their contribution to the peer review of this work. Primary Handling Editors: Joe Aslin, Heike Langenberg.

**Reprints and permission information** is available at <http://www.nature.com/reprints>

**Publisher's note** Springer Nature remains neutral with regard to jurisdictional claims in published maps and institutional affiliations.



**Open Access** This article is licensed under a Creative Commons Attribution 4.0 International License, which permits use, sharing, adaptation, distribution and reproduction in any medium or format, as long as you give appropriate credit to the original author(s) and the source, provide a link to the Creative Commons license, and indicate if changes were made. The images or other third party material in this article are included in the article's Creative Commons license, unless indicated otherwise in a credit line to the material. If material is not included in the article's Creative Commons license and your intended use is not permitted by statutory regulation or exceeds the permitted use, you will need to obtain permission directly from the copyright holder. To view a copy of this license, visit <http://creativecommons.org/licenses/by/4.0/>.

© The Author(s) 2021